RSC Advances

ROYAL SOCIETY OF CHEMISTRY

www.rsc.org/advances

Journal Name

RSCPublishing

ARTICLE

Synthesis of mesoporous ZSM-5 catalysts using different mesogenous templates and the application in methanol conversion for enhanced catalyst lifespan

Cite this: DOI: 10.1039/x0xx00000x

Received 00th January 2012,
Accepted 00th January 2012

DOI: 10.1039/x0xx00000x

www.rsc.org/

Quanyi Wang, [a,b,e] Shutao Xu, [a] Jingrun Chen, [a,e] Yingxu Wei, [a,*] Jinzhe Li, [a] Dong Fan, [a,e] Zhengxi Yu, [a] Yue Qi, [a] Yanli He, [a] Shuliang Xu, [a] Cuiyu Yuan, [a] You Zhou, [a,e] Jinbang Wang, [a] Mozhi Zhang, [a,e] Baolian Su, [b,c,*] and Zhongmin Liu [a,d,*]

In this work, two kinds of mesoporous ZSM-5 were synthesized successfully via a hydrothermal method by the utilization of different soft templates - dimethyl octadecyl [3 - (trimethoxysilyl) propyl] ammonium chloride ($[(CH_3O)_3SiC_3H_6N(CH_3)_2C_{18}H_{37}]Cl$, TPOAC) and hexadecyl trimethyl ammonium bromide ($C_{16}H_{33}(CH_3)_3NBr$，CTAB). The obtained mesoporous ZSM-5 samples were compared with conventional ZSM-5 and the effect of different surfactant usage during the synthesis of mesoporous ZSM-5 on the physicochemical and catalytic properties were systematically investigated. Multiple techniques, such as XRD, SEM, N_2 adsorption techniques, HP ^{129}Xe NMR, ^{27}Al MAS NMR, ^{29}Si MAS NMR, and ^{1}H MAS NMR, were employed in characterization. Even the synthesized mesoporous ZSM-5 samples were with equal surface area, they presented different relative crystallinity, morphologies, pore size distributions, micropore-mesopore interconnectivity, framework atom coordination states and acidity. When using these synthesized ZSM-5 samples as the catalysts of methanol conversion, the mesoporous ZSM-5 templated with TPOAC exhibited extremely long catalyst lifespan compared with conventional ZSM-5, while mesoporous ZSM-5 templated with CTAB showed no advantage in the catalyst lifetime prolongation during the reaction. The differences in the catalytic lifespan and reduction of coke deposition were correlated to the variation of acidity and porosity with the mesopore generation in the ZSM-5 catalysts by the usage of different structure directing agents. Compared to the mesopore structure directing agent, CTAB, with the use of TPOAC as the template and part of Si source, mesoporous ZSM-5 could be synthesized with good mesopore-micropore interconnectivity, which accounted for the improved catalytic performance in the reaction of methanol conversion.

1. Introduction

ZSM-5 has been a very important shape selective acid catalyst in the petrochemical industry over the past decades due to its excellent properties, such as high surface area, high hydrothermal stability, intrinsic acidity, well-defined microporosity, and the ability to confine active species. [1-3] However, the microporosity in itself often leads to intra-crystalline diffusion limitations, which severely hinder its practical applications in the processing or transformation of the feedstock with large size and also in the reaction with short lifetime caused by severe coke deposition. [3-8] To overcome the disadvantages resulted by the pure microporosity in ZSM-5, two different strategies have been developed in recent years. The first strategy is to reduce the crystal size of ZSM-5 or prepare the nanosized ZSM-5. [9,10] The lessening of the zeolite crystal size from the level of micrometer to nanometer scale could decrease the diffusion path length and improve the molecular diffusion, which is conducive to the enhancement of catalytic activity. However, this method is restricted from application by the complicated crystallization process and the difficulty of separating nano-sized zeolite crystal from the synthesis system. [9] The second strategy is to prepare ZSM-5 with both micropore and mesopore systems, which are usually referred to mesoporous ZSM-5 or hierarchical ZSM-5. [11-13] The bimodal porous ZSM-5 is supposed to combine the benefits of each sole pore size regime, which is of great potential to improve the efficiency of zeolite catalysis, enhance the accessibility to active sites, and reduce the intra-crystalline diffusion obstacle. [14] Mesoporous ZSM-5 has been supposed to be the potential catalyst in the conversion of heavy oil to light olefins and light olefins production through MTO reaction via non-petrochemical route, especially under the background of the shortage of oil resource. [15-17]

Considerable efforts have been contributed to the introduction of mesopores into ZSM-5 and up to now, a wide variety of synthesis strategies have been proposed. In the previous studies, various post-treatment methods, including heat treatment, [18,19] steaming treatment, [20,21] acid leaching, [20,21] alkaline leaching, [22,23] and other chemical treatment, [24] have been proved to be efficient in creating mesopores in ZSM-5 crystals. However, it is hard to create uniform mesopores

in these ways. Furthermore, the loss of relative crystallinity and the partial dissolution of the parent zeolite cannot be avoided during these processes. [3-8] Another one of the strategies for synthesizing ZSM-5 crystals containing mesopores is by means of crystallization using a hard templating method, which involves the use of porous or hollow solids as matrices and fabricate mesoporous ZSM-5 within their cavities. [8] For the hard templating method, carbon nanoparticles or nanotubes, [12,25-27] poly(methyl methacrylate) (PMMA) nanospheres, [28] nano $CaCO_3$, [29] and polymer beads, [30,31] have been successfully employed as mesogenous templates to create mesopores in ZSM-5. But unfortunately, inconvenient multi-steps were usually needed for this method owing to the incompatibility between hard templates and precursor sources. [32,33] Thus in recent years, dual templating method, with combined usage of structure directing agent for the synthesis of ZSM-5 (i.e. TPAOH) and various soft mesogeneous templates for the synthesis of mesophase, such as cationic surfactant (CTAB), [34] nonionic alkyl poly (ethylene oxide) surfactants, [32] organosiliane, [35] cationic polymer, [36] silylated polymer, [37] natural product, [33] etc. has been drawn tremendous attention for its high efficiency in creating mesopores in ZSM-5. However, under most circumstances, the two different templating systems, i.e. the ZSM-5 template and the mesopore structure directing agent, worked in a competitive, rather than a cooperative manner, which may resulted in the formation of a physical mixture containing amorphous mesoporous material and bulk zeolite without mesoporosity. [38] To address this issue, a specially designed amphiphilic organosilane template ($[(CH_3O)_3\text{-}SiC_3H_6\text{-}N(CH_3)_2C_nH_{2n+1}]^+Cl^-$, TPOAC), which can work as both silicon source and mesopore directing agents, was introduced by Ryoo in 2006. [39] The synthesized ZSM-5 was highly mesoporous and the mesopore diameter could be tuned by the chain length of TPOAC and the synthesis temperature. More recently, Ryoo et al. made a new progress in the synthesis of mesoporous ZSM-5 by the usage of an organic surfactant equipped with a multi-ammonium headgroup. [40-44] The multi-ammonium headgroup can direct the crystallization of microporous zeolites, while the numerous surfactant molecules were assembled into a micelle that can direct various mesoporous structures. This indicated that this kind of organic surfactant equipped with a multi-ammonium headgroup could serve as both zeolitic templates and mesogenous structure directing agents. For example, $[C_{22}H_{45}\text{-}N^+(CH_3)_2\text{-}C_6H_{12}\text{-}N^+(CH_3)_2\text{-}C_6H_{13}][Br]_2$ was reported be used to generate ZSM-5 nanosheets with single-unit-cell thickness of 2.5 nm. [40] Subsequently, this strategy was also applied to the synthesis of ZSM-5 nanosponge and MFI-like zeolite with hexagonally ordered mesopores. [44]

The catalytic applications of mesoporous ZSM-5 have been undoubtedly important and intensively studied in the past decade. Different types of acid catalysis reactions, such as alkylation, catalytic cracking, and methanol conversion, have been widely investigated by the use of mesoporous ZSM-5 as catalysts. [5,45-47] Christensen et al. [10] reported the use of mesoporous ZSM-5 as the catalyst in the gas phase alkylation of benzene with ethylene gave rise to higher conversion and higher selectivity towards ethyl benzene than conventional ZSM-5. Sun and Prins [48] investigated the alkylation of benzene with benzyl alcohol using mesoporous ZSM-5 as catalyst and the results exhibited dramatically improved catalytic activity over mesoporous ZSM-5 as compared with conventional ZSM-5. The use of mesoporous ZSM-5 as the catalyst was also reported to be helpful in the prolongation of lifetime in the alkylation reaction beside the improvement of reaction activity. [49] When Bjørgen et al. [50] tested methanol to gasoline reaction (MTG) over mesoporous ZSM-5 prepared by alkaline treatment, a prolonged lifetime compared to conventional ZSM-5 could be found. Recently, Ryoo and co-workers [40,44] investigated MTG over mesoporous ZSM-5 with the thickness of only one single unit cell (2 nm) and the catalytic performance also presented a significant increase in catalyst lifetime compared to conventional ZSM-5.

In the present work, two kinds of mesoporous ZSM-5 were synthesized successfully via a hydrothermal method by the utilization of two different soft templates - TPOAC and CTAB. The microporous ZSM-5 and the mesoporous ZSM-5 samples were well characterized adopting multi-type techniques, including XRD, SEM, N_2 adsorption and desorption, HP ^{129}Xe NMR, ^{29}Si MAS NMR, ^{27}Al MAS NMR, and ^{1}H MAS NMR. Methanol conversions were performed by employing all these samples as the catalysts. Our main objective is to shed light on the influence of mesoporosity development, resulted from the use of different mesogenous templates, on the physicochemical characters and catalytic properties of these materials through comparison. Based on the above-mentioned work, the improvement of catalyst stability and reduction of coke formation during methanol conversion over mesoporous ZSM-5 were explained by correlating the catalytic performance to the variation of acidity and porosity with the mesopore generation in the catalysts.

2. Experimental

2.1 Chemical reagents

All the chemical reagents in this article [Tetraethyl orthosilicate (TEOS, 98.0%, Tianjin Kermel Chemical Co. Ltd), Sodium metaaluminate ($NaAlO_2$, 41 wt% Al_2O_3, Sinopharm Chemcial Reagent Co. Ltd), Sodium hydroxide (NaOH, 96.0%, Tianjin Kermel Chemical Co. Ltd), Tetrapropylammonium bromide (TPABr, 98.0%, Aladdin reagent), Hexadecyl trimethyl ammonium Bromide (CTAB, 99.0%, Tianjin Kermel Chemical Co. Ltd), Dimethyl octadecyl [3 - (trimethoxysilyl) propyl] ammonium chloride ($[(CH_3O)_3SiC_3H_6N(CH_3)_2C_{18}H_{37}]Cl$, TPOAC, 65%, Aladdin reagent), Methanol (99.5%, Tianjin Kermel Chemical Co. Ltd), and Perfluorotributylamine (analytical standard, Sigma-Aldrich)] were commercial products of analytical grade, and were used as received without any further purification.

2.2 Preparation of catalysts

Conventional and mesoporous ZSM-5 samples were synthesized by a hydrothermal method with modified synthesis procedure according to the work reported previously. [34,39,44] For the synthesis of conventional ZSM-5, the final molar composition of the synthesis mixture was 40 SiO_2 : 1.0 Al_2O_3 : 20 NaOH : 10 TPABr : 7000 H_2O. For the synthesis of mesoporous ZSM-5 zeolite (MZSM-5-A and MZSM-5-B), TPOAC and CTAB were added to the conventional synthesis mixture, and the final molar composition of the synthesis mixture was 38.4 SiO_2 : 1.0 Al_2O_3 : 20 NaOH : 10 TPABr : 1.6 TPOAC : 7000 H_2O for MZSM-5-A and 40 SiO_2 : 1.0 Al_2O_3 : 20 NaOH : 10 TPABr : 4.0 CTAB : 7000 H_2O for MZSM-5-B.

In the typical synthesis procedure for MZSM-5-A, 0.26g $NaAlO_2$, 0.80g NaOH, and 2.80g TPABr were firstly dissolved in 135g H_2O. Then, 8.57g TEOS and 1.20 g TPOAC were added into the synthesis gel to make a mixture under agitation. For the synthesis of MZSM-5-B, 8.57g TEOS and 1.20 g TPOAC in the synthesis gel of MZSM-5-A were substituted by 8.93 g TEOS and 1.52g CTAB. For the synthesis of conventional ZSM-5, only 8.93 g TEOS was added in the second step. All the above-mentioned synthesis mixtures were transferred into 200 ml Teflon-lined stainless steel pressure vessels, sealed and heated in ovens at 150 ℃ under autogenic pressure. After crystallization, the as-synthesized samples were washed, centrifugally separated, and dried at 120 ℃ for 12 h. In order to remove the organic template, the as-synthesized samples were calcined at 550℃ for 8 h. The H-type ZSM-5 were obtained by

transferring the calcined samples into NH_4^+ form with four times ion-exchange in 1.0 M NH_4NO_3 solution at 80℃ and subsequent calcinations of the NH_4^+ form samples at 550℃ for 8 h.

2.3 Characterizations of materials

X-ray diffraction (XRD) patterns were obtained with a D/max-rb X-ray diffractometer, using Cu Kα radiation (λ=1.5405Å) at room temperature with instrumental settings of 30~40 kV and 40 mA. The relative crystallinity was calculated based on the intensity of the peaks with 2θ = 22°~25°. Scanning electron microscopy (SEM) images were obtained for morphological identification using a Hitachi S-3400N electron microscope. High resolution transmission electron microscopies (HR-TEM) were performed using a JEM-2100 transmission electron microscope. N_2 adsorption and desorption experiments were performed at 77K on NOVA 4000 gas adsorption analyzer (Quantachrome Corp.). Each sample was evacuated at 403 K for 1 h and then at 623 K for 3 h before adsorption.

Laser-hyperpolarized (HP) ^{129}Xe NMR experiments were carried out at 110.6 MHz on Varian Infinity-plus 400 spectrometer using a 7.5 mm probe. Before each experiment, samples (60-80 mesh) were dehydrated at 673 K under vacuum (<10^{-5} Torr) for 24 h. Optical polarization of xenon was achieved with a homemade apparatus with the optical pumping cell in the fringe field of the spectrometer magnet and 60 W diode laser array (Coherent FAP-System). A flow of gas mixture (1% Xe-1% N_2-98% He) was delivered at the rate of 100-150 mL/min to the sample in detection region via plastic tubing. Variable-temperature NMR measurements were performed in the range of 153-293 K. All one-dimensional spectra were acquired with 3.0 μs π/2 pulse, 100-200 scans, and 2 s recycle delay. The chemical shifts were referenced to the signal of xenon gas. Although the line of the xenon gas is temperature dependence, generally chemical shifts vary no more than 1 ppm in the temperature range of the experiments.

^{29}Si, ^{27}Al, and ^{1}H MAS NMR measurements were performed on 600 MHz Bruker Avance III equipped with a 4 mm MAS probe. ^{29}Si MAS NMR spectra were recorded using high-power proton decoupling with a spinning rate of 10 kHz. A 1024 scans were accumulated with a π/2 pulse width of 3 μs and a 10 s recycle delay. The chemical shifts were referenced to DSS (4, 4-dimethyl-4-silapentane sulfonate sodium) at 0 ppm. ^{27}Al MAS NMR spectra were recorded using one pulse sequence with a spinning rate of 12 kHz. A 100 scans were accumulated with a π/8 pulse width of 0.75 μs and a 2 s recycle delay. The chemical shifts were referenced to $(NH_4)Al(SO_4)_2{\cdot}12H_2O$ at -0.4 ppm. ^{1}H MAS NMR spectra were recorded using a 4 mm MAS probe. The pulse width was 2.2 μs for a π/4 pulse, and 32 scans were accumulated with a 10 s recycle delay. Samples were spun at 12 kHz, and chemical shifts were referenced to adamantane at 1.74 ppm. For the determination of quantitative results, all samples were weighed, and the spectra were calibrated by measuring a known amount of adamantane performed under the same conditions. Before ^{1}H MAS NMR measurements of adsorption of perfluorotributylamine on ZSM-5-based samples, the samples were dehydrated typically at 693 K under pressure below 10^{-3} Pa for 20 h before adsorption. Selective adsorption of perfluorotributylamine was performed by exposing the dehydrated sample to saturated vapor at room temperature for 30 min. After equilibration, the samples were degassed at 298 K to remove the physical adsorbate on the surface. The software Dmfit was employed for deconvolution using fitting of Gaussian-Lorentzian lineshapes.

2.4 Catalytic tests

Catalytic conversions of methanol (continuous flow reaction) were performed in a quartz tubular fixed-bed reactor at atmospheric pressure. The catalyst (100 mg, 60-80 mesh) loaded in the quartz reactor was activated at 500 ℃ in a He flow of 30 mL/min for 1 h before starting each reaction run and then the temperature was adjusted to reaction temperature of 450 ℃. The methanol was fed by passing the carrier gas (24 mL/min) through a saturator containing methanol at 33 ℃, which gave a WHSV of 6.0 h^{-1}. The reaction products were analyzed using an on-line gas chromatograph (Agilent GC 7890N), equipped with a flame ionization detector (FID) and a capillary column of HP-PONA. The products with time on stream of 220 min were also analyzed by a gas chromatograph (Bruker 450-GC) equipped with a flame ionization detector (FID) and a capillary column of HP-PLOT Q. The conversion and selectivity were calculated on CH_2 basis. Dimethyl ether (DME) was considered as reactant in the calculation.

The amount of generated coke in ZSM-5 catalysts after the reactions of methanol was determined by thermal analysis (TG-DTA) on a TA SDTQ600 analyzer at the temperature range of 50-800 ℃ with the heating rate of 10 ℃/min under an air flow of 100 ml/min.

3. Results and discussion

3.1 Crystalline and morphology

The low-angle and the wide-angle XRD patterns of the synthesized conventional ZSM-5 and the mesoporous ZSM-5 samples, MZSM-5-A and MZSM-5-B, are compared in Fig. S1 (see supporting information) and Fig. 1, respectively. As indicated in Fig. S1, there is only one peak with low intensity for MZSM-5-A and MZSM-5-B, which implies the generation of mesopores in them. Furthermore, the intrinsic lattice structure of MFI topology is observed in Fig. 1 for all the three samples, but the relative crystallinity of MFI phase is quite different. The conventional ZSM-5 sample has the highest relative crystallinity among the three samples. The relative crystallinity of MZSM-5-A is a little lower than that of conventional ZSM-5, but higher than that of MZSM-5-B. Meanwhile, peak broadening in the patterns of MZSM-5-A and MZSM-5-B are also reflected in Fig. 1 as compared with conventional ZSM-5.

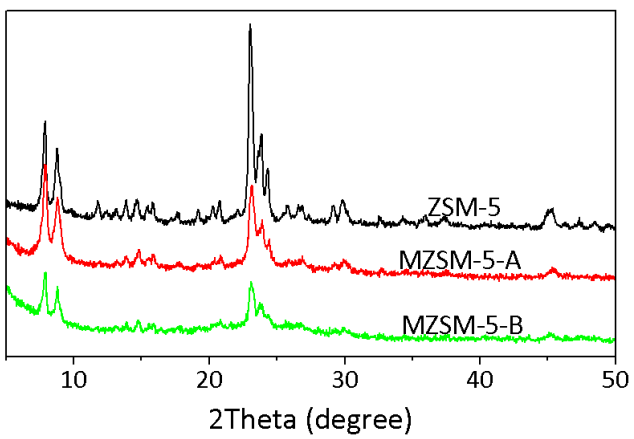

Fig. 1 XRD patterns of the synthesized conventional ZSM-5, MZSM-5-A, and MZSM-5-B.

The representative SEM images given in Fig. 2 show that conventional ZSM-5, MZSM-5-A, and MZSM-5-B are bulk particles with different size. The bulk particle size for conventional ZSM-5, MZSM-5-A, and MZSM-5-B are around 1 μm, 400 nm, and 800 nm, respectively. Furthermore, the surface of the bulk particles for conventional ZSM-5 seems to be very smooth. Differently, the surfaces of the bulk particles for MZSM-5-A and MZSM-5-B are rougher than that of conventional ZSM-5, as a consequence of

mesopore generation in their particles. In addition, it should be mentioned that very little amount of amorphous substances exist between the bulk particles of MZSM-5-B. The existence of the amorphous phase may also result in the lowest relative crystallinity of MZSM-5-B among the three samples.

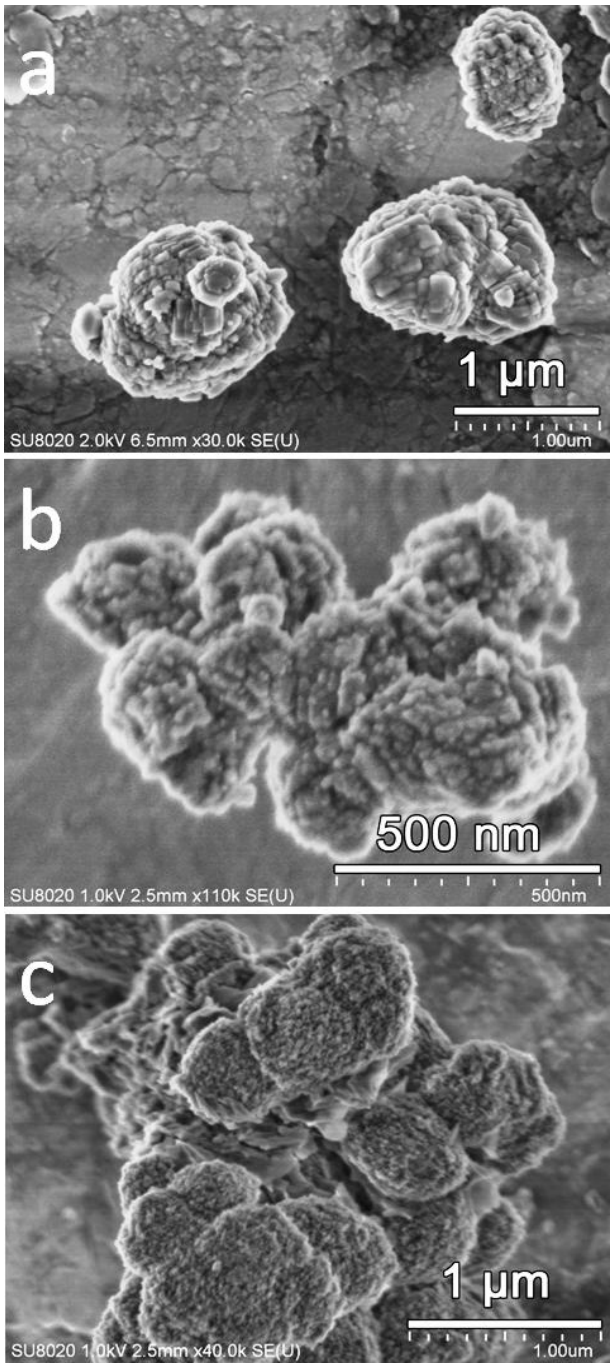

Fig. 2 SEM images of the synthesized samples: (a) conventional ZSM-5, (b) MZSM-5-A, and (c) MZSM-5-B.

TEM and HR-TEM were also employed to gain further insight into the structures of the synthesized samples. Fig. 3(a) is a typical TEM image of conventional ZSM-5. Here one can see that the bulk particles of conventional ZSM-5 are assembled from the fusion of crystals, which seemed to be in good accordance with the SEM characterization. However, owing to the thickness of conventional ZSM-5 particles, it was difficult to have a good contrast to observe the arrangement as seen in SEM. An HR-TEM image (Fig. 3(b)), the enlargement of the conventional ZSM-5 crystals in Fig. 3(a), reveals clear lattice fringes. This indicates that the synthesized conventional ZSM-5 is highly crystallized, in agreement with the XRD data. Fig. 3(c) is a representative TEM image of MZSM-5-A at low magnification. As was clearly illustrated in the image, the morphology of MZSM-5-A is confirmed, and the particles of MZSM-5-A have the same contrast. The contrast of MZSM-5-A is better than that of conventional ZSM-5. Fig. 3(d) gives a HR-TEM image of the MZSM-5-A particles locating at the edge as seen in Fig. 3(c) with higher resolution. Clear lattice fringes also exhibit, indicating that MZSM-5-A is also highly crystallized. The TEM image of MZSM-5-B is presented in Fig. 3(e), which is similar to that of MZSM-5-A. As is also demonstrated in Fig. 3(e), the bulk particles of MZSM-5-B have the close contrast as those of MZSM-5-A. In addition, a little amount of amorphous phase or mesoporous phase is observed in Fig. 3(e), which is well consistent with the SEM characterization. Furthermore, the lattice fringe presented in the HR-TEM image of MZSM-5-B (Fig. 3(f)) confirms the crystallized phase of MZSM-5-B.

3.2 Porosity and micropore-mesopore interconnectivity

The N_2 adsorption and desorption isotherms of the conventional ZSM-5 and the mesoporous ZSM-5 samples, MZSM-5-A and MZSM-5-B, are presented in Fig. 4(a). The curves of pore size distribution, which are calculated from adsorption branch using the Barrett-Joyner-Halenda (BJH) model, are compared in Fig. 4(b). The BET surface area and total pore volume are given in Table 1. As shown in Fig. 4(a), the conventional ZSM-5 sample presents a representative Type I (Langmuir) isotherm according to the classification of IUPAC, with no obvious N_2 adsorption amount increase and no distinct hysteresis loop at high relative pressure, which is characteristic of microporous materials without mesoporosity. This is also confirmed by the pore size distribution curve in Fig. 4(b).

While for the mesoporous ZSM-5 samples, MZSM-5-A and MZSM-5-B, the N_2 adsorption and desorption isotherms are greatly different from that of the conventional ZSM-5. The N_2 adsorption and desorption isotherms of MZSM-5-A and MZSM-5-B in Fig. 4(a) give a notably isotherm with mixed types, Type I and Type IV, indicating the existence of both micropores and mesopores. Simultaneously, a dramatic increase in the adsorption amounts at high relative pressure and a hysteresis loop caused by possible generation of mesopores are also observed. MZSM-5-A and MZSM-5-B have very close BET surface area, 502 m^2/g and 508 m^2/g, respectively. The increased BET surface area and pore volume come from the enhanced porosity in the range of mesopore (see Table 1). For MZSM-5-A, the mesoporous surface area is 350 m^2/g, and the mesoporous volume is 0.34 cm^3/g and these values for MZSM-5-B are 421 m^2/g and 0.45 cm^3/g, respectively. However, the gain in mesoporosity of MZSM-5-A and MZSM-5-B is accompanied with the loss of microporosity. Compared to conventional ZSM-5 with microporous surface area of 269 m^2/g, the microporous surface area decreased to 152 m^2/g and 87 m^2/g for the two mesoporous ZSM-5, respectively. The microporous volume is also reduced with the generation of mesopores.

As shown in Fig. 4(b), the mesopore size of MZSM-5-A and MZSM-5-B is centered around 3.0 nm. The relatively high peak intensity implies more mesopores formation in MZSM-5-B

than MZSM-5-A, corresponding to their difference in mesoporous surface area and volume. Considering the same starting gel composition and identical synthesis condition, the difference of the mesopore generation in MZSM-5-A and MZSM-5-B are more possibly related with the different mesogenous template usage in the synthesis.

The HP ^{129}Xe NMR spectroscopy is a powerful tool for studying the porosity of porous materials. The observed ^{129}Xe chemical shift, reflecting mainly the interactions between xenon atoms and the surface, is very sensitive to the geometry and can also represent the connectivity and uniformity of the porosity.[51-54] Therefore, continuous-flow HP ^{129}Xe NMR was employed herein to study the micropore-mesopore interconnectivity of the synthesized samples.

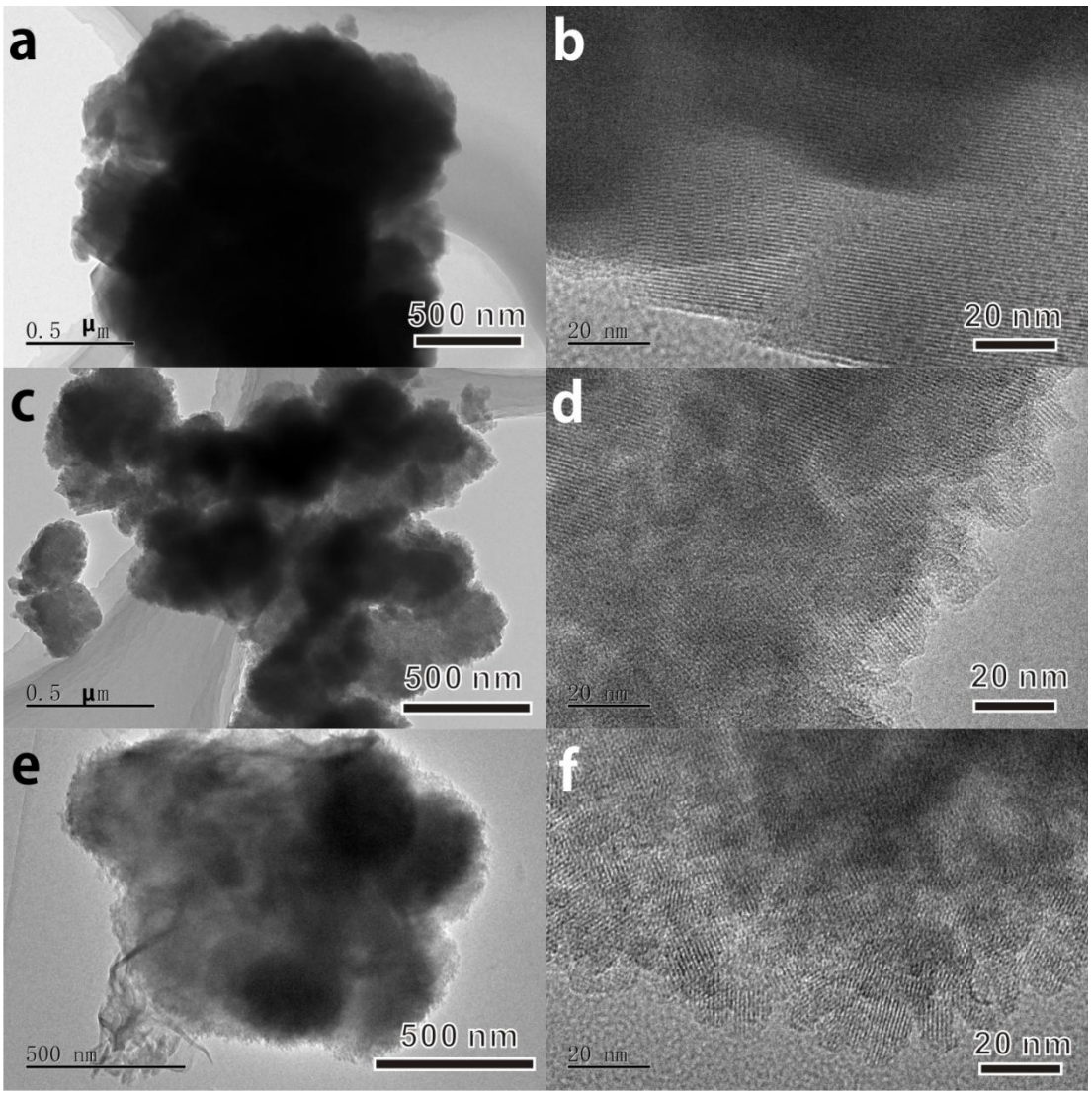

Fig. 3 Typical TEM images and HR-TEM images of the synthesized samples: (a) TEM image of conventional ZSM-5, (b) HR-TEM image of conventional ZSM-5, (c) TEM image of MZSM-5-A, (d) HR-TEM image of MZSM-5-A, (e) TEM image of MZSM-5-B, and (f) HR-TEM image of MZSM-5-B.

Table 1 The textural properties and the SiO_2/Al_2O_3 ratio of conventional ZSM-5, MZSM-5-A, and MZSM-5-B.

Samples	Surface area (m^2/g)			Pore volume (cm^3/g)			SiO_2/Al_2O_3[g]
	S_{BET}[a]	S_{Meso}[b]	S_{Micro}[c]	V_{Total}[d]	V_{Meso}[e]	V_{Micro}[f]	
ZSM-5	328	59	269	0.16	0.03	0.13	45
MZSM-5-A	502	350	152	0.41	0.34	0.07	45
MZSM-5-B	508	421	87	0.49	0.45	0.04	40

[a] BET surface area. [b] $S_{Meso} = S_{BET} - S_{Micro}$. [c] t-plot micropore surface area. [d] Pore volume at $p/p_0 = 0.99$. [e] $V_{Meso} = V_{Total} - V_{micro}$. [f] t-plot micropore volume. [g] Determined by ^{29}Si MAS NMR.

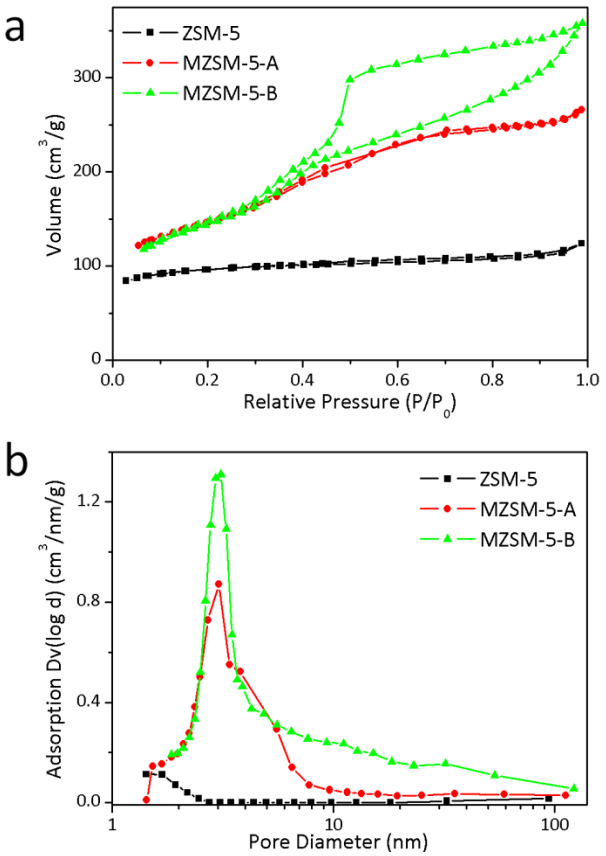

Fig. 4 (a) N_2 adsorption/desorption isotherms and (b) BJH pore size distributions (adsorption branch) of conventional ZSM-5, MZSM-5-A, and MZSM-5-B.

The variable-temperature HP ^{129}Xe NMR spectra of conventional ZSM-5, MZSM-5-A, and MZSM-5-B are shown in Fig. 5. For all the samples, the serial of peaks at 0 ppm is from xenon in the gas phase. Only one downfield signal, line A (116-186 ppm), could be observed in the spectra of conventional ZSM-5 from 293 to 153 K, which is ascribed to the xenon adsorbed in the 10-membered ring channel of ZSM-5. Meanwhile, the chemical shifts of line A increase with cooling the sample from 293 to 153 K. This is a normal trend for porous materials in variable-temperature HP ^{129}Xe NMR experiments, mainly resulted from the increased interaction of the Xe and zeolite surface, as well as Xe-Xe interactions at lower temperatures. [52,53]

For the mesoporous samples MZSM-5-A and MZSM-5-B, the temperature-dependent behavior of line A in Fig. 5 is similar to that of conventional ZSM-5, implying that the microporosity maintains in mesoporous ZSM-5 samples. Beside line A, in Fig. 5(b) and 5(c), a new upfield series of signals, line B appears at low temperature range, from 173 to 153 K in the ^{129}Xe NMR spectra of MZSM-5-A and from 193 to 153 K in the ^{129}Xe NMR spectra of MZSM-5-B, and the chemical shifts go to downfield with temperature decrease. Low temperature ^{129}Xe NMR spectra can be used to discriminate different pore environments, especially the mesoporosity. [52,53] The appearance of line A and line B represents more than one type of pore environments in MZSM-5-A and MZSM-5-B. Taking the N_2 physical adsorption measurements into account, the new upfield line B at low temperature may come from Xe adsorbed in the mesopores of MZSM-5-A and MZSM-5-B. At relatively high temperature range, above 193 K or 213 K for MZSM-5-A and MZSM-5-B, fast exchange of Xe between the micropores and the mesopores in the two samples leads to the preferential adsorption of xenon in the micropores rather than in the mesopores, so the series of signal of line B representing the Xe adsorption in mesopore disappear.

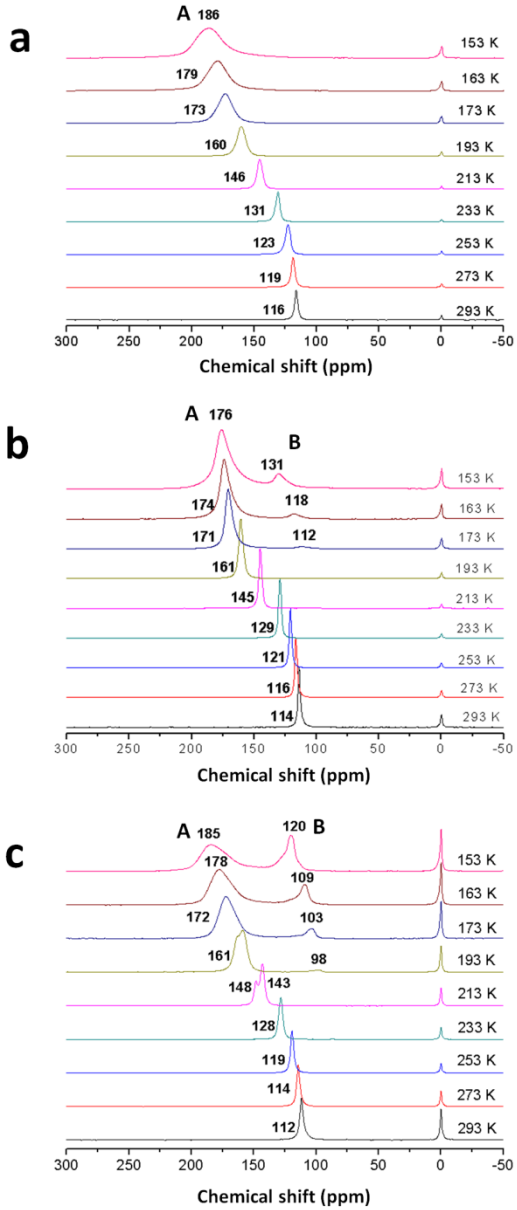

Fig. 5 Laser-hyperpolarized ^{129}Xe NMR spectra of Xe adsorbed in (a) conventional ZSM-5, (b) MZSM-5-A, and (c) MZSM-5-B. The temperature is varied from 293 to 153 K.

Moreover, one can see that line B in the spectra of MZSM-5-A shows relatively larger chemical shifts than those in the spectra of MZSM-5-B. The chemical shift difference ($\Delta\delta$) of xenon between microporous and mesoporous domains can be used to estimate the pore connectivity. [52,53] The chemical shift difference ($\Delta\delta$) of xenon of MZSM-5-A and MZSM-5-B at temperatures of 173, 163, and 153 K is compared in Fig. 6. The $\Delta\delta$ values of MZSM-5-A, with chemical shift difference of 59, 56, and 45 ppm, are always lower than those of MZSM-5-B, with $\Delta\delta$ values of 69, 69, and 65 ppm, indicating that the faster Xe exchange between micropores and

mesopores in MZSM-5-A than in MZSM-5-B. This also demonstrates that MZSM-5-A possesses better interconnectivity between micropores and mesopores than MZSM-5-B.

Based on the above observations, even the mesopores can be generated in the synthesized ZSM-5 samples, the usage of different mesopore directing agents in the starting synthesis mixtures results in the difference in the interconnectivity between micropores and mesopores, which may further give rise to the differences in catalytic performances.

3.3 Chemical environments of silicon and aluminum atoms

The ^{29}Si MAS NMR and ^{27}Al MAS NMR were employed to determine the local coordination environment of silicon and aluminum and the SiO_2/Al_2O_3 ratio. Fig. 7 illustrates the ^{29}Si MAS NMR spectra of conventional ZSM-5, MZSM-5-A, and MZSM-5-B. Four peaks are recorded in the spectrum of conventional ZSM-5 after deconvolution. The peaks at -113 and -107 ppm are related to Si(0Al) (Q^4) and 3Si(1Al) species respectively. The signal at -117 ppm is attributed to the crystallographically inequivalent Si(0Al) (Q^4) sites, while the signal with low intensity at -100 ppm is normally associated with silanol group ($(SiO)_3SiOH$, Q^3). [22] Compared with conventional ZSM-5, in the spectra of MZSM-5-A and MZSM-5-B, the peaks at -113, -117 and -107 ppm representing two Si(0Al) and 3Si(1Al) species also appear in high intensity. Differently, the two silanol groups, $(SiO)_3SiOH$ (Q^3) and $(SiO)_2Si(OH)_2$ (Q^2), at -100 and -93 ppm, which present very low intensity or is absent in the spectrum of conventional ZSM-5, appear with relatively high intensity in the spectra of MZSM-5-A and MZSM-5-B. The large amounts of silanol groups possibly come from the mesoporous surface in MZSM-5-A and MZSM-5-B.

The SiO_2/Al_2O_3 ratios of ZSM-5, MZSM-5-A and MZSM-5-B calculated based on the ^{29}Si MAS NMR spectra are listed in Table 1. The SiO_2/Al_2O_3 ratios of ZSM-5 and MZSM-5-A are both slightly higher than that of the synthesis gel and the SiO_2/Al_2O_3 ratio of MZSM-5-B is very close to that of the synthesis gel.

^{27}Al MAS NMR spectra of all the three samples are illustrated in Fig. 8. Two peaks appear in the spectrum of conventional ZSM-5. One peak centered at ~55 ppm corresponds to the tetrahedral aluminum from framework aluminum species. The other peak, centered at ~0 ppm with low intensity, is ascribed to the octahedral aluminum, which is generally associated with the non-framework aluminum species. The generation of mesopores in ZSM-5 gives rise to the intensity increase of the signal at 0 ppm, corresponding to the reduction of relative crystallinity in the XRD patterns. One new peak centered at ~27 ppm was also observed in MZSM-5-A and MZSM-5-B, which can be attributed to pentacoordinated aluminum species. [55-57] The pentacoordinated aluminum species may be associated with the framework Al species perturbed by the less ordered environments of mesoporous ZSM-5 samples.

The calculation of the peak widths of the tetrahedral Al at their half height can provide information on the homogeneity of the Al environments. As calculated from Fig. 7, the peak widths of the tetrahedral Al at half height for conventional ZSM-5, MZSM-5-A, and MZSM-5-B are 998 Hz, 1338 Hz, and 1731 Hz, respectively, which also imply the homogeneity of the tetrahedral Al environments. The proportions of the extraframework Al for conventional ZSM-5, MZSM-5-A, and MZSM-5-B are 10%, 18%, and 23%, respectively, indicating the sequence of the extraframework Al follows MZSM-5-B > MZSM-5-A > conventional ZSM-5. Compared to the MZSM-5-B using CTAB as mesopore directing agent, MZSM-5-A synthesized by the addition of TPOAC into the synthesis gel possesses the lower amount of non-framework Al species.

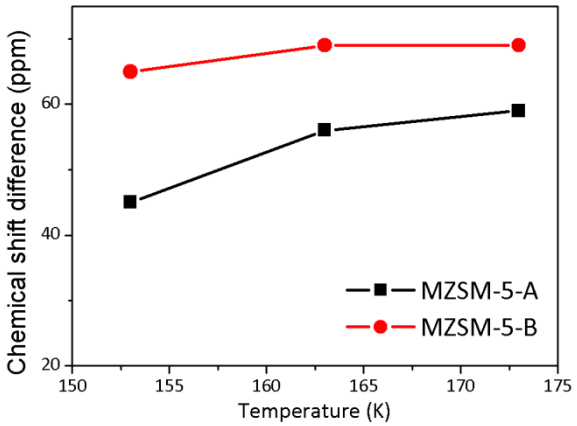

Fig. 6 The chemical shift difference ($\Delta\delta$) of xenon signal from microporous and mesoporous domains of MZSM-5-A and MZSM-5-B with temperature.

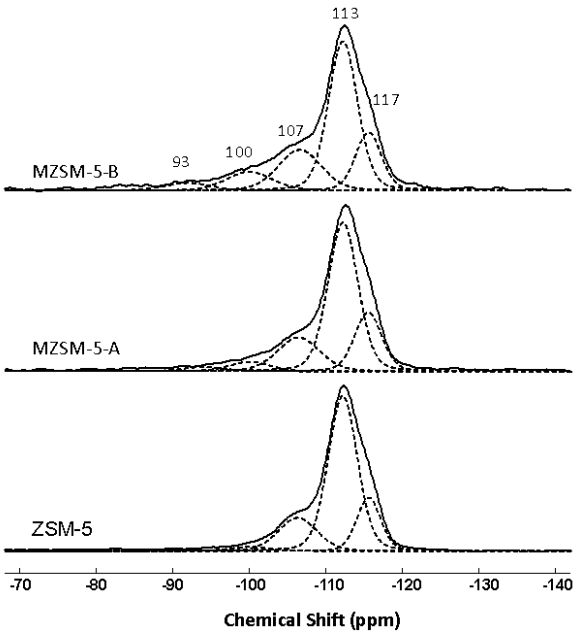

Fig. 7 ^{29}Si MAS NMR spectra of conventional ZSM-5, MZSM-5-A, and MZSM-5-B.

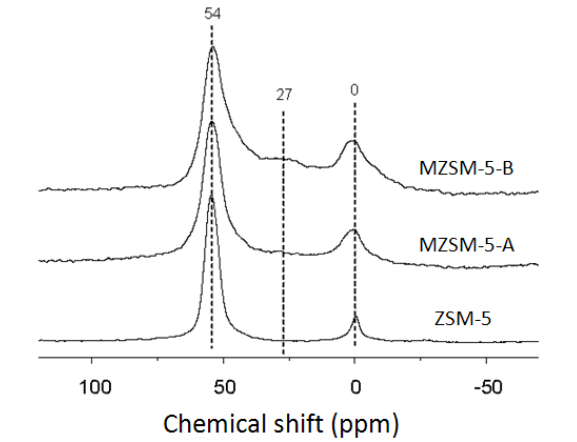

Fig. 8 ^{27}Al MAS NMR spectra of conventional ZSM-5, MZSM-5-A, and MZSM-5-B.

Table 2. The results of the quantified concentration of hydroxyl groups and Brönsted acid after deconvolution.

Samples	B acid (II) (mmol/g)	B acid (I) (mmol/g)	Total B acid (mmol/g)	AlOH (mmol/g)	SiOH (mmol/g)	External B acid sites / Total B acid sites (%)
ZSM-5	0.095	0.14	0.235	0.123	0.038	9
MZSM-5-A	0.041	0.082	0.123	0.144	0.223	36
MZSM-5-B	0.058	0.063	0.121	0.129	0.390	33

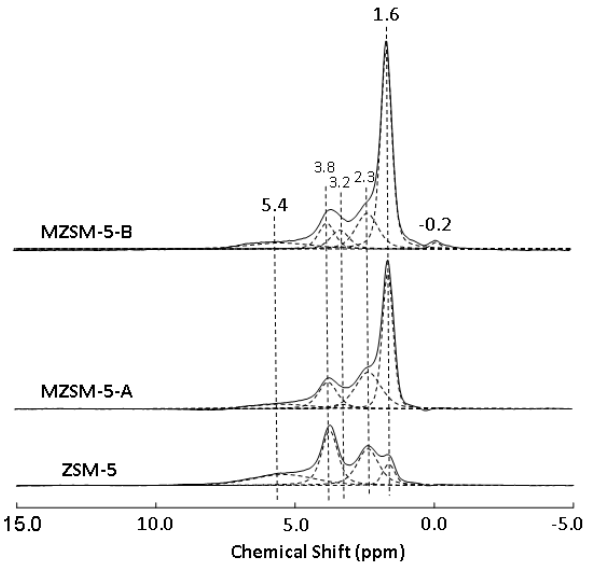

Fig. 9 ^{1}H MAS NMR spectra of conventional ZSM-5, MZSM-5-A and MZSM-5-B.

3.4 ^{1}H solid state NMR and acidity measurements

The ^{1}H MAS NMR spectra of ZSM-5, MZSM-5-A, and MZSM-5-B are shown in Fig. 9, and the results after a quantitative deconvolution of the corresponding spectra are also plotted. For all the three samples, four peaks with the chemical shift of 1.6, 2.3, 3.8 and 5.4 ppm can be clearly resolved, as reported previously. [58] The signals at 2.3 and 1.6 ppm are attributed to aluminum hydroxyls (Al-OH) species with hydrogen bond effect and silanol group (Si-OH), respectively.

The signals at 3.8 and 5.4 ppm are associated with two kind of bridge hydroxyl species (Si(OH)Al), corresponding to the Brönsted acid sites (I), which locates at the intersection position of the channels, and the Brönsted acid sites (II), the restricted Brönsted acid sites which is influenced by additional electrostatic interaction of the zeolite framework. [59-61] The results of the quantified concentration of hydroxyl groups with the signal intensity are listed in Table 2.

Even all the OH species are found in MZSM-5-A and MZSM-5-B, when compared with conventional ZSM-5 (see Fig. 9), the Si-OH and Al-OH species present relatively high intensity for mesoporous ZSM-5 samples. Especially in the spectrum of MZSM-5-B, the intensity of Si-OH species at 1.6 ppm is very high. In addition, a new signal at 3.2 ppm in the spectrum of MZSM-5-B is also observed and probably originated from the silanol groups with hydrogen bond effect. [62] These observations indicate that the Si-OH species are more predominantly formed over the surface of mesoporous ZSM-5 samples than the other hydroxyl groups. At the same time, the concentration of bridging hydroxyl groups reduces greatly in intensity. The intensity variation of surface hydroxyl groups demonstrates that the generation of mesopores in the catalysts of MZSM-5-A and MZSM-5-B results in the reduction of Brönsted acid sites concentration and intensification of the surface Al-OH and Si-OH species. This is well consistent with the results of ^{29}Si and ^{27}Al MAS NMR measurements with the detection of relatively large amount of Q^2, Q^3 and octahedral aluminum species. Total Brönsted acid concentration is 0.235 mmol/g over the conventional ZSM-5 sample, while this value is reduced to 0.123 and 0.121 mmol/g over MZSM-5-A and MZSM-5-B. Based on these results, it can be concluded that there is no remarkable difference in the concentration of Brönsted acid sites between the two mesoporous ZSM-5 samples while their textural properties and the Brönsted acid sites (location at I or II) vary substantially.

Perfluorotributylamine [$(n\text{-}C_4F_9)_3N$], a weak basic probe molecule with a diameter of 0.94 nm which is much larger than the pore opening of ZSM-5, has been utilized to quantify the external acidity of the catalysts, [63] and then the ^{1}H MAS NMR spectra of ZSM-5-based catalysts before and after $(n\text{-}C_4F_9)_3N$ adsorption were recorded. As exhibited in Table 2, the external Brönsted acid sites of ZSM-5 accounts for 9% of the total Brönsted acid sites, while for the mesoporous catalysts, MZSM-5-A and MZSM-5-B, the external Brönsted acid sites attain to 36% and 33% of the total Brönsted acid sites, respectively. With the generation of mesopores in the ZSM-5 catalyst, more acid sites are located on the mesoporous surface, which are more accessible than the acid sites located in the 10-membered ring channel of conventional ZSM-5.

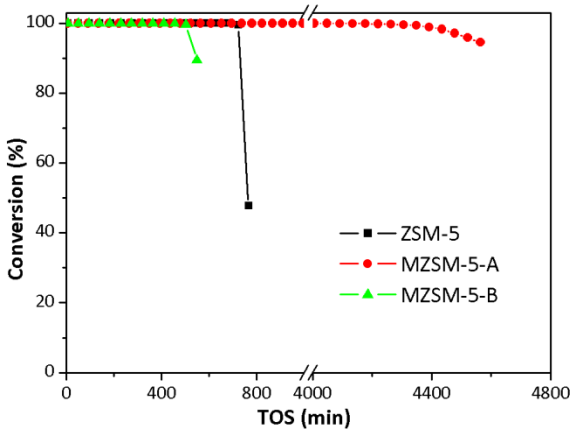

Fig. 10 Conversion of methanol (continuous flow reaction) over conventional ZSM-5, MZSM-5-A, and MZSM-5-B.

3.5 Catalytic tests of methanol conversion over the synthesized ZSM-5 catalysts

Catalytic performances of methanol conversion over the conventional ZSM-5 and the mesoporous ZSM-5 catalysts, MZSM-5-A and MZSM-5-B were evaluated on a continuous flow fixed-bed

quartz tubular reactor at 450 ℃ and the methanol conversion and the product selectivity are detailed in Fig. 10 and Table 3, respectively.

The conversion evolution as a function of reaction time shows that the conversion of methanol is 100% for all the three ZSM-5-based catalysts at the beginning period of the reaction, indicating the high initial activity of all the three catalysts, but the catalyst lifetime, during which 100% methanol conversion can be kept varies considerably by the usage of different catalysts. As clearly indicated in Fig. 10, 100% methanol conversion can be kept for more than 677 min over conventional ZSM-5, while for the catalyst of MZSM-5-A with hierarchical porosity, 100% methanol conversion can maintain for more than 4048 min, indicating the long-term stability of this catalyst. Surprisingly, when the reaction is performed over MZSM-5-B, the deactivation occurs after time-on-stream of 455 min, the shortest catalyst lifetime among the three samples.

Catalyst lifetime is influenced by multiple factors. Beside reaction conditions, crystal size, catalyst acidity, textural structure may also have effect on the long-term reaction stability of methanol conversion. In the present work, the variation of catalyst acidity and porosity may play more important roles in the long-term stability of methanol conversion.

Table 3 The selectivity of the generated aliphatic hydrocarbons and aromatic hydrocarbons over conventional ZSM-5, MZSM-5-A, and MZSM-5-B during methanol conversion (continuous flow reaction, time on stream=220 min).

Product distribution		ZSM-5	MZSM-5-A	MZSM-5-B
Aliphatic hydrocarbons (%)	CH_4	2.76	0.71	2.30
	C_2H_4	10.63	11.83	13.36
	C_2H_6	0.52	0.15	0.18
	C_3H_6	14.59	20.83	24.04
	C_3H_8	10.42	4.60	3.45
	C_4H_8	5.79	8.24	10.59
	C_4H_{10}	16.64	15.67	12.42
	C_5^+	9.89	17.74	15.89
	total	71.24	79.77	82.23
Aromatic hydrocarbons (%)	Benzene	2.06	0.83	0.61
	Toluene	8.20	3.99	3.50
	Xylene	13.70	8.42	8.99
	TriMB	3.21	5.13	2.89
	TetraMB	0.54	1.25	0.77
	PentaMB	0.03	0.19	0.31
	HexaMB	0.00	0.07	0.23
	MN	0.35	0.08	0.11
	DiMN	0.58	0.17	0.18
	TriMN	0.09	0.06	0.11
	TetraMN	0.00	0.03	0.06
	total	28.76	20.22	17.76

TriMB: Trimethylbenzene; TetraMB: Tetramethylbenzene; PentaMB: Pentamethylbenzene; HexaMB: Hexamethylbenzene; MN: Methylnaphthalene; DiMN: Dimethylnaphthalene; TriMN: Trimethylnaphthalene; TetraMN: Tetramethylnaphthalene.

The generated products over the three ZSM-5 catalysts are composed of aliphatic hydrocarbons and aromatic products. As depicted in Table 3, for all the three catalysts, paraffins and olefins, such as CH_4, C_2H_4, C_2H_6, C_3H_6, C_3H_8, C_4H_8, C_4H_{10}, C_5 and hydrocarbons higher than C_5 (C_5^+), appear as the aliphatic hydrocarbon products and benzene, methylbenzenes and methylnaphthalenes appear as the aromatic products. All the generated products over the three ZSM-5-based catalysts keep stable selectivity with time on stream before the occurrence of the deactivation (See supporting information Fig. S2). Compared to conventional ZSM-5, with aliphatic hydrocarbon selectivity of 71.24% and aromatics selectivity of 28.76%, when using the mesoporous ZSM-5 samples as the catalysts, aliphatic hydrocarbons selectivity is improved and aromatic products generation is depressed to some extent. The selectivity of aliphatic hydrocarbons and aromatics are 79.77% and 20.22% for MZSM-5-A, and these values for MZSM-5-B are 82.23% and 17.76% respectively. Detailed results show that when the reaction is performed over mesoporous ZSM-5, especially over MZSM-5-B, the selectivity of light alkenes, including C_2H_4, C_3H_6, and C_4H_8, is enhanced, as well as the obvious reduced selectivity of light alkanes, such as CH_4, C_2H_6, and C_3H_8. The increase of C_4 products (butenes and butanes) selectivity and the dramatic selectivity enhancement of hydrocarbons higher than C_5 (C_5^+) over MZSM-5-A and MZSM-5-B indicate that the generation of mesopores in the ZSM-5 catalysts causes predominant formation of the hydrocarbon with relatively big size. Aromatic products are usually regarded as the secondary products of methanol conversion. When the reactive olefins generate over the ZSM-5 catalysts, their further transformation, such as oligomerization, cyclization and hydrogen transfer, will produce the aromatic products over the acid zeolite catalysts.[64,65] Lowered acid concentration of MZSM-5-A and MZSM-5-B compared to conventional ZSM-5 is very helpful for

depressing the secondary reaction for aromatics generation. This also partially explains the lower aromatics selectivity of aromatics compounds among the products over mesoporous ZSM-5 catalysts. Furthermore, the generation of mesopores and the interconnectivity between the 10-membered ring channel and the mesopores of the mesoporous samples, proved by HP ^{129}Xe NMR, give rise to the great improvement of mass transfer of the products, especially the diffusion of olefins and aromatics products. The quick leaving of these reactive products will also prevent them from the further transformation to the aromatic products. Detailed results of aromatic product generation present great differences in product distribution between mesoporous ZSM-5 and conventional ZSM-5 catalyst. Over conventional ZSM-5, benzene and lower methylbenzene, such as toluene, xylene and trimethylbenzenes appear as the main aromatic products, higher methylbenzenes generate with low selectivity. But over mesoporous ZSM-5 catalysts, MZSM-5-A and MZSM-5-B, among the generated aromatic products, trimethylbenzenes and tetramethylbenezenes generate with higher selectivity than the conventional ZSM-5 catalyst. Interestingly, the higher methylbenzenes, pentamethylbenzene and hexamethylbenzene, which almost cannot be detected among the effluent products over the conventional ZSM-5 catalyst, appear in the volatile phase of the reaction over the two mespoporous ZSM-5 catalysts. At the same time, big size methyl-substituted naphthalenes, such as trimethylnaphthalenes and tetramethylnapthalenes also appear. With the generation of mesopores in the ZSM-5 catalysts, the acid sites located at the interconnection of 10-membered ring pore and mesopores or acid sites at the pore mouth of 10-membered ring pore and open to the external surface of the mesoporous ZSM-5 catalysts may work as the reaction center for the generation of the products with big size.

After reaction, the catalysts were discharged and the coke deposited over the three deactivated catalysts was measured by thermal analysis. As detailed in Table 4, the weight loss from the combustion of the retained coke species is 14.05%, 23.71% and 8.35% for conventional ZSM-5, MZSM-5-A and MZSM-5-B, respectively. Due to the deactivation occurrence at different time on stream, such as 100% methanol conversion maintains for 677 min over conventional ZSM-5, 4048 min over MZSM-5-A, and 455 min over MZSM-5-B, the amount of the coke deposited on the three catalysts corresponds to different duration of methanol conversion. In the present work, the portion of reactant cost on coke generation is also evaluated with the consideration of different catalyst lifetime and total feeding amount of methanol during the reaction. The fraction of methanol consumption on coke formation (P_{coke}) in the present work is described as (1). Methanol feeding is calculated on CH_2 basis. P_{coke} of the three catalysts are compared in Table 4 together with the coke amount measured with thermal analysis.

$$P_{coke}\ (mg/g) = \text{coke amount (mg)/methanol feedstock (g)} \quad (1)$$

Even the catalyst of MZSM-5-A presents the highest coke amount (23.71%) after methanol conversion, the fraction of methanol consumption on coke over this catalyst is much lower than those of conventional ZSM-5 and MZSM-5-B. This means the cost of methanol feedstock on coke deposition over MZSM-5-A is lower than the other two catalysts. Slight coke deposition ensures the operation of long-term methanol conversion and makes MZSM-5-A a very effective catalyst of methanol conversion with high activity and stability for hydrocarbon production. The generation of mesopore in the ZSM-5 catalyst and the good interconnectivity of the mesopores and the micropores in MZSM-5-A catalyst, confirmed by the HP ^{129}Xe NMR, contribute to the great improvement of mass transfer of the reactant and the generated products. Compared to the conventional ZSM-5, the reduction of the diffusion obstacle of the generated hydrocarbon products in MZSM-5-A avoids the severe secondary transformation of the active products, especially the reaction of generated olefins and aromatics products to form the heavy hydrocarbon residue in the catalyst, in this way, coke formation is largely depressed. For the case of MZSM-5-B, even mesopores can be also formed, the low relative crystallinity and high mesoporous surface indicate only portion of this material processes the crystallized structure of ZSM-5. More importantly, due to the poor interconnectivity of mesopores and micropores in MZSM-5-B as indicated in Fig. 5, the microporous ZSM-5 and mesoporous phase may work separately during MTO reaction, therefore the long-term methanol conversion cannot be realized without the improvement in reactant and product diffusion as MZSM-5-A, in addition to the lower acid concentration, the MZSM-5-B presents the shortest lifetime in methanol conversion among the three catalysts.

Table 4 The variation of coke formation in methanol conversion over conventional ZSM-5, MZSM-5-A, and MZSM-5-B.

Catalysts	ZSM-5	MZSM-5-A	MZSM-5-B
Coke (%, g/gcat)	14.05	23.71	8.35
P_{coke} (mg/gMeOH, CH_2 basis)	0.0908	0.0256	0.0803

The mesoporous structure generation and the interconnectivity of bimodal pore structure play an important role in the prolongation of the catalyst lifespan and the hydrocarbon product generation. The differences of porous structure generation between the two mesoporous catalysts originate from the synthesis procedure with the usage of different structure directing agents. When CTAB was used as the structure directing agent for mesopore generation, together with template of TPABr for MFI structure generation, MZSM-5-B was synthesized. Unfortunately, as indicated in the measurements of XRD, N_2 physical adsorption and NMR, the MZSM-5-B processes the lowest relative crystallinity of ZSM-5 and lowest microporous surface. The separation of the crystalline phase with MFI topology and the amorphous phase with mesoporous structure made it an inefficient catalyst in methanol conversion. TPOAC, an amphiphilic organosilane, beside its function as a super-molecular template for the generation of mesopore in the MZSM-5-A, it can also act as part of silica source and can be incorporated into the MFI framework of MZSM-5-A. The two cooperative functions working together contribute not only to the mesopore generation, but also to the good interconnectivity of micropores and mesopores in the MZSM-5-A catalyst.

The comparisons of the methanol conversion and product generation on the conventional ZSM-5 and the mesoporous ZSM-5, MZSM-5-A, are depicted in Scheme 1. The conventional ZSM-5 catalyst deactivation stems from the acid site coverage or channel blockage with coke formation. The generation of mesopores interconnective to the narrow 10-membered ring channel of ZSM-5 gives rise to remarkable enhancement in mass transfer of reactant and generated products. The acid sites in the MZSM-5-A catalyst are more accessible than the conventional ZSM-5 catalyst during methanol conversion, which confirms the catalytic efficiency of the catalyst. At the same time, quick leaving of generated products also reduces the occurrence of the further reaction of the active products to form the sterically demanding coke

species, which can block the acid sites and channels and cause the deactivation of the catalyst. Therefore, the longest catalyst lifespan and highest reaction stability are observed over the mesoporous ZSM-5 catalyst, MZSM-5-A.

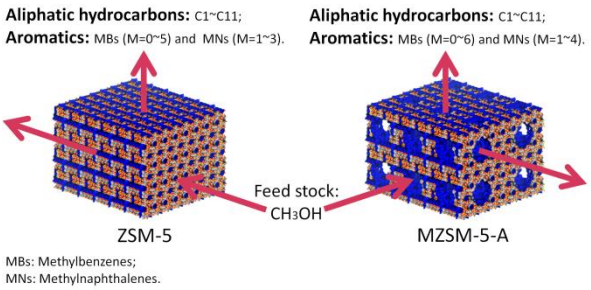

Scheme 1 The proposed schematic description of methanol conversion over conventional ZSM-5 and MZSM-5-A.

4. Conclusion

Two kinds of mesoporous ZSM-5 samples were successfully synthesized via a hydrothermal method by the utilization of different mesogenous templates - TPOAC and CTAB. N_2 physical adsorption measurement proved the mesoporous structure generation in MZSM-5-A and MZSM-5-B. Compared to conventional ZSM-5, the two mesoporous ZSM-5 samples presented intrinsic lattice structure of MFI topology, but with relatively low crystallinity. The generation of mesopores gave rise to the intensification of the silanol groups and the reduction of bridge hydroxyl groups on the surface, so the Brönsted acid concentration of these two mesoporous ZSM-5 samples was lowered. The usage of different mesogenous templates during the synthesis procedure resulted in the difference in the mesopore-micropore interconnectivity between the two synthesized mesoporous ZSM-5 catalysts with bimodal pore structure. In comparison with the mesoporous ZSM-5 using CTAB as the mesogeneous template, the mesoporous ZSM-5 templated from TPOAC presented more excellent interconnectivity between micropores and mesopores beside its higher relative crystallinity. Catalytic transformation of methanol over the three ZSM-5-based catalysts generated aliphatic hydrocarbons and aromatic hydrocarbons and these products selectivity kept stable with time on stream during the reaction. The mesoporous ZSM-5 catalyst templated with TPOAC exhibited the longest lifetime during methanol conversion compared with the mesoporous ZSM-5 templated with CTAB and the conventional ZSM-5 catalyst. The catalyst deactivation and catalyst lifetime were strongly dependent on the porosity variation resulted by the introduction of mesopores in ZSM-5 catalysts. For the mesoporous ZSM-5 catalyst templated with CTAB, the separation of the crystalline phase with MFI topology and the mesoporous phase made it an inefficient catalyst in methanol conversion. TPOAC, beside its function as a super-molecular template for the generation of mesopore in the mesoporous ZSM-5, it could also act as part of silica source and could be incorporated into the MFI framework. The two cooperative functions working together contributed not only to the uniform mesopore generation, but also to the good interconnectivity of micropores and mesopores in the catalyst. The good mesopore-micropore interconnectivity of MZSM-5-A catalyst greatly promoted the mass transfer of the reactant and generated products and reduced the coke deposition. The slight coke deposition over this catalyst during methanol conversion ensured the long-term operation of methanol conversion with high reactivity.

Acknowledgements

We thank the National Natural Science Foundation of China (No. 21273230, 21273005, 21103176, and 21103180) for financial support of this work. B.L. Su acknowledges the Chinese Central Government for an "Expert of the State" position in the program of "Thousands Talents" and the Chinese Ministry of Education for a Changjiang Scholar position at the Wuhan University of Technology.

Notes and references

[a] Dalian National Laboratory for Clean Energy, Dalian Institute of Chemical Physics, Chinese Academy of Sciences, 457 Zhongshan Road, Dalian 116023, PR China * Corresponding authors: liuzm@dicp.ac.cn; weiyx@dicp.ac.cn; tel. 0086-411-84379335; Fax: 0086-411-84691570

[b] Laboratory of Inorganic Materials Chemistry (CMI), University of Namur (FUNDP), 61 rue de Bruxelles, B-5000 Namur, Belgium. * Corresponding author: bao-lian.su@fundp.ac.be

[c] State key Laboratory of Advanced technology for Materials Synthesis and Processing, Wuhan University of Technology, 122 Luoshi Road, 430070, Wuhan, Hubei, China. * Corresponding author: baoliansu@whut.edu.cn

[d] State Key Laboratory of Catalysis, Dalian Institute of Chemical Physics, Chinese Academy of Sciences, Dalian 116023, China

[e] University of Chinese Academy of Sciences, Beijing, 100049, China

Electronic Supplementary Information (ESI) available: [The low angle XRD patterns of the mesoporous ZSM-5 samples. The selectivity of the generated products over ZSM-5, MZSM-5-A, and MZSM-5-B during methanol conversion (continuous flow reaction, experimental conditions: WHSV = 6 h^{-1}, T = 723 K, catalyst weight = 100 mg.).]. See DOI: 10.1039/b000000x/

1 M. Milina, S. Mitchell, N. L. Michels, J. Kenvin, J. Pérez-Ramírez, *J. Catal.* 2013, **308**, 398-407.
2 L. Zhao, B. J. Shen, J. S. Gao, C. M. Xu, *J. Catal.* 2008, **258**, 228-234.
3 J. C. Groen, L. A. A. Peffer, J. A. Moulijn, J. Pérez-Ramírez, *J. Mater. Chem.* 2006, **16**, 2121-2131.
4 K. Na, M. Choi, R. Ryoo, *Micro. Mesopor. Mater.* 2013, **166**, 3-19.
5 Y. S.Tao, H. Kanoh, L. Abrams, K. Kaneko, *Chem. Rev.* 2006, **106**, 896-910.
6 A. Corma, *Chem. Rev.* 1997, **97**, 2373-2420.
7 R. Chal, C. Gérardin, M. Bulut, S. van Donk, *ChemCatChem* 2011, **3**, 67-81.
8 D. P. Serrano, J. M. Escola, P. Pizarro, *Chem. Soc. Rev.* 2013, **42**, 4004-4035.
9 L. Tosheva, V. P. Valtchev, *Chem. Mater.* 2005, **17**, 2494-2513.
10 C. H. Christensen, K. Johannsen, I. Schmidt, C. H. Christensen, *J. Am. Chem. Soc.* 2003, **125**, 13370-13371.
11 S. S. Kim, J. Shah, T. J. Pinnavaia, *Chem. Mater.* 2003, **15**, 1664-1668.
12 Y. S. Tao, H. Kanoh, K. Kaneko, *J. Am. Chem. Soc.* 2003, **125**, 6044-6045.

13 D. P. Serrano, J. Aguado, J. M. Escola, J. M. Rodríguez, Á. Peral, *Chem. Mater.* 2006, **18**, 2462-2464.
14 G. S. Zhu, S. L. Qiu, F. F. Gao, D. S. Li, Y. F. Li, R. W. Wang, B. Gao, B. S. Li, Y. H. Guo, R. R. Xu, Z. Liu, O. Terasaki, *J. Mater. Chem.* 2001, **11**, 1687-1693.
15 M. Stöcker, *Micropor. Mesopor. Mater.* 1999, **29**, 3-48.
16 J. Z. Li, Y. X. Wei, J. R. Chen, P. Tian, X. Su, S. T. Xu, Y. Qi, Q. Y. Wang, Y. Zhou, Y. L. He, Z. M. Liu, *J. Am. Chem. Soc.* 2012, **134**, 836-839.
17 S. T. Xu, A. M. Zheng, Y. X. Wei, J. R. Chen, J. Z. Li, Y. Y. Chu, M. Z. Zhang, Q. Y. Wang, Y. Zhou, J. B. Wang, F. Deng, Z. M. Liu, *Angew. Chem. Int. Ed.* 2013, **52**, 11564 -11568.
18 C. M. Zhang, Q. Liu, Z. Xu, *Micropor. Mesopor. Mater.* 2003, **62**, 157-163.
19 C. M. Zhang, Z. Xu, K. S. Wan, *Appl. Catal. A* 2004, **258**, 55-61.
20 V. Nagabhatla, K. Manoj, *Micropor. Mesopor. Mater.* 2006, **92**, 31-37.
21 A. E. W. Beers, J. A. van Bokhoven, K. M. de Lathouder, *J. Catal.* 2003, **218**, 239-248.
22 L. L. Su, L. Liu, J. Q. Zhuang, , X. H. Bao *Catal. Lett.* 2003, **91**, 155-167.
23 J. C. Groen, T. Bach, U. Ziese, A. M. P. van Donk, K. P. de Jong, J. A. Moulijin, J. Pérez-Ramírez, *J. Am. Chem. Soc.* 2005, **127**, 10792-10793.
24 C. S. Triantafillidis, A. G. Vlessidis, N. P. Evmiridis, *Ind. Eng. Chem. Res.* 2000, **39**, 307-319.
25 C. J. H. Jacobsen, C. Madsen, J. Houzvicka, I. Schmidt, A. Carlsson, *J. Am. Chem. Soc.* 2000, **122**, 7116-7117.
26 Z. Yang, Y. Xia, R. Mokaya, *Adv. Mater.* 2004, **16**, 727-732.
27 Y. S. Tao, Y. Hattori, A. Matumoto, H. Kanoh, K. Kaneko, *J. Phys. Chem. B* 2005, **109**, 194-199.
28 J. J. Zhao, J. Zhou, Y. Chen, Q. He, M. L. Ruan, L. M. Guo, J. L. Shi, H. R. Chen, *J. Mater. Chem.* 2009, **19**, 7614-7616.
29 H. B. Zhu, Z. C. Liu, Y. D. Wang, D. J. Kong, X. H. Yuan, Z. K. Xie, *Chem. Mater.* 2008, **20**, 1134-1139.
30 H. Zhang, G. C. Hardy, Y. Z. Khimyak, M. J. Rosseinsky, A. I. Cooper, *Chem. Mater.* 2004, **16**, 4245-4256.
31 B. T. Holland, L. Abrams, A. Stein, *J. Am. Chem. Soc.* 1999, **121**, 4308-4309.
32 J. Zhou, Z. L. Hua, Z. C. Liu, W. Wu, Y. Zhu, J. L. Shi, *ACS Catal.* 2011, **1**, 287-291.
33 J. J. Jin, X. D. Zhang, Y. S. Li, H. Li, W. Wu, Y. L. Cui, Q. Chen, L. Li, J. L. Gu, W. R. Zhao, J. L. Shi, *Chem. Eur. J.* 2012, **18**, 16549-16555.
34 Y. Zhu, Z. L. Hua, J. Zhou, L. Wang, J. Zhao, Y. Gong, W. Wu, M. Ruan, J. L. Shi, *Chem.-Eur. J.* 2011, **17**, 14618-14627.
35 D. P. Serrano, R. A. García, G. Vicente, M. Linares, D. Procházková, J. Čejka, *J. Catal.* 2011, **279**, 366-380.
36 J. Song, L. Ren, C. Yin, Y. Ji, Z. Wu, J. Li, F. S. Xiao, *J. Phys. Chem. C* 2008, **112**, 8609-8613.
37 H. Wang, T. J. Pinnavaia, *Angew. Chem., Int. Ed.* 2006, **45**, 7603-7606.
38 V. N. Shetti, J. Kim, R. Srivastava, M. Choi, R. Ryoo, *J. Catal.* 2008, **254**, 296-303.
39 M. Choi, H. S. Choi, R. Srivastava, C. Venkatesan, D. H. Choi, R. Ryoo, *Nat. Mater.* 2006, **5**, 718-723.
40 M. Choi, K. Na, J. Kim, Y. Sakamoto, O. Terasaki, R. Ryoo, *Nature* 2009, **461**, 246-249.
41 K. Na, M. Choi, W. Park, Y. Sakamoto, O. Terasaki, R. Ryoo, *J. Am. Chem. Soc.* 2010, **132**, 4169-4177.
42 K. Na, W. Park, Y. Seo, R. Ryoo, *Chem. Mater.* 2011, **23**, 1273-1279.
43 K. Na, C. Jo, J. Kim, W. S. Ahn, R. Ryoo, *ACS Catal.* 2011, **1**, 901-907.
44 K. Na, C. Jo, J. Kim, K. Cho, J. Jung, Y. Seo, R. J. Messinger, B. F. Chmelka, R. Ryoo, Science 2011, **333**, 328-332.
45 J. Čejka, *Catal. Rev. -Sci. Eng.* 2007, **49**, 457-509.
46 Z.L. Hua, J. Zhou, J. L. Shi, *Chem. Comm.* 2011, **47**, 10536-10547.
47 M. S. Holm, E. Taarning, K. Egeblad, C. H. Christensen, *Catal. Today* 2011, **168**, 3-16.
48 Y. Sun, R. Prins, *Appl. Catal. A* 2008, **336**, 11-16.
49 L. Jin, X. Zhou, H. Hu, B. Ma, *Catal. Commun.* 2008, **10**, 336-340.
50 M. Bjørgen, F. Joensen, M. S. Holm, U. Olsbye, K. P. Lillerud, S. Svelle, *Appl. Catal. A* 2008, **345**, 43-50.
51 I. L. Moudrakovski, V. V. Terskikh, C. I. Ratcliffe, J. A. Ripmeester, *J. Phys. Chem. B* 2002, **106** , 5938-5946.
52 Y. Liu, W. P. Zhang, X. W. Han, X. H. Bao, *Chin. J. Catal.* 2006, **27**, 827-836.
53 Y. Liu, W. P. Zhang, Z. C. Liu, S. T. Xu, Y. D. Wang, Z. K. Xie, X. W. Han, X. H. Bao, *J. Phys. Chem. C* 2008, **112**, 15375-15381.
54 S. T. Xu, W. P. Zhang, X. C. Liu, X. W. Han, X. H. Bao, *J. Am. Chem. Soc.* 2009, **131**, 13722-13727.
55 P. Sazama, B. Wichterlova, J. Dedecek, Z. Tvaruzkova, Z. Musilova, L. Palumbo, S. Sklenak, O. Gonsiorova, *Micropor. Mesopor. Mater.* 2011, **143**, 87-96.
56 L. B. Alemany, G. W. Kirker, *J. Am. Chem. Soc.* 1986, **108**, 6158-6162.
57 W. P. Zhang, D. Ma, X. W. Han, X. M. Liu, X. H. Bao, X. W. Guo, X. S. Wang, *J. Catal.* 1999, **188**, 393-402.
58 D. Ma, Y. Shu, W. Zhang, X. Han, Y. Xu, X. Bao, *Angew. Chem., Int. Ed.* 2000, **39**, 2928-2931.
59 M. Hunger, S. Ernst, S. Steuernagel, J. Weitkamp, *Micropor. Mater.* 1996, **6**, 349-353.
60 M. Hunger, *Catal. Rev.: Sci. Eng.* 1997, **39**, 345-393.
61 L. W. Beck, J. L. White, J. F. Haw, *J. Am. Chem. Soc.* 1994, **116**, 9657-9661.
62 W. P. Zhang, C. I. Ratcliffe, I. L. Moudrakovski, J. S. Tsea, C. Y. Mou, J. A. Ripmeestera, *Micropor. Mesopor. Mater.* 2005, **79**, 195-203.
63 W. P. Zhang, D. Ma, X. C. Liu, X. M. Liu, X. H. Bao, *Chem. Commun.* 1999, **12**, 1091-1092.
64 C. Y. Yuan, Y. X. Wei, J. Z. Li, S. T. Xu, J. R. Chen, Y. Zhou, Q. Y. Wang, L. Xu, Z. M. Liu, *Chin. J. Catal.* 2012, **33**, 367-374.
65 C. Y. Yuan, Y. X. Wei, L. Xu, J. Z. Li, S. T. Xu, Y. Zhou, J. R. Chen, Q. Y. Wang, Z. M. Liu, *Chin. J. Catal.* 2012, **33**, 768-770.

